IET Electric Power Applications

Research Article

Coupled circuit analysis of the brushless doubly fed machine using the winding function theory

ISSN 1751-8660
Received on 6th November 2019
Revised 6th April 2020
Accepted on 20th April 2020
doi: 10.1049/iet-epa.2019.0915
www.ietdl.org

Oreoluwa I. Olubamiwa[1], Nkosinathi Gule[1] ✉, Maarten J. Kamper[1]

[1]*Electrical Machines Laboratory, Department of Electrical & Electronic Engineering, Stellenbosch University, Private Bag X1, Matieland 7602, South Africa*

✉ *E-mail: nathie@sun.ac.za*

Abstract: The brushless doubly fed induction machine (BDFM) is considered as an alternative to doubly fed induction generators (DFIGs) in wind energy conversion systems. However, BDFMs have a complex machine structure, and their operations are relatively complicated. In this study, the winding function theory is used in the development of a coupled circuit (CC) model for BDFMs with nested loop (NL) and cage+NL rotors, in order to give a robust representation of the electrical operations of BDFMs. The electrical circuit analysis of BDFMs having NL and cage+NL rotors is comprehensively detailed, with the stator and rotor inductances calculated using their winding functions. The interactions of BDFM rotor loops with stator windings are demonstrated in terms of mutual inductances. CC models of different BDFMs are simulated for synchronous doubly fed BDFM operations with an emphasis on generating regions. Also, fresh insight into the torque production in BDFMs is provided, with the rotor loops and stator winding contributions to torque magnitude and ripple examined.

1 Introduction

Brushless doubly fed (induction) machines (BDFMs) can be used in wind energy conversion systems in a similar way to doubly fed induction generators (DFIGs). BDFMs utilise fractionally rated converters, and are capable of synchronous torque operations with power factor control, just as in DFIGs [1]. BDFMs also have superior intrinsic low-voltage ride through characteristics compared to DFIGs [2]. With slip ring and brush failures being a primary cause for downtimes in DFIGs as reported in [3], the absence of brushes and slip rings makes BDFMs a potential alternative to DFIGs.

BDFMs have two stator windings; the power winding (PW) with p_1 pole pairs, and the control winding (CW) with p_2 pole pairs. The PW and CW are wound such that $p_1 \neq p_2$ to prevent the direct coupling between them. The stator windings are cross-coupled via a specially designed rotor. Although a number of rotor topologies have been proposed for BDFMs, the nested loop (NL) and cage +NL rotors with $p_1 + p_2$ nests are the most popular. The NL and cage+NL rotors have robust structures with lower flux leakages and losses compared to the other potential rotor types. Also, NL and cage+NL rotors are easier to manufacture [1, 4, 5].

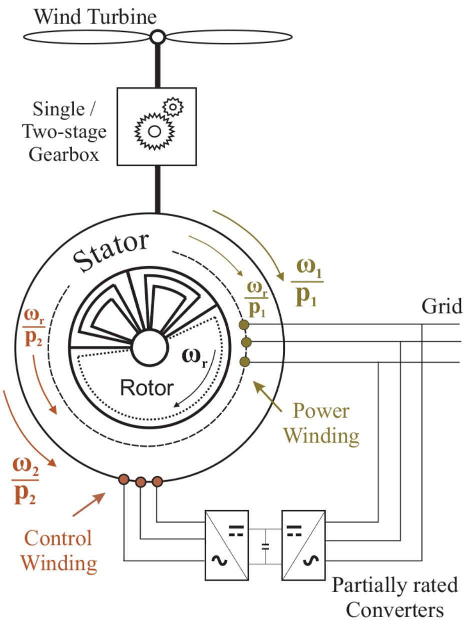

Fig. 1 *BDFM-based wind turbine drivetrain*

When BDFMs are operated in the synchronous doubly fed mode, which is desirable in wind power applications, the PW and CW produce rotating independent magnetic fields travelling in opposite directions [1]. These fields induce currents on the rotor which have the same frequency and phase delay in the rotor nests. The rotor currents consequently produce a magnetic field with two main harmonic components corresponding to the pole pairs of the PW and CW, which couple the windings, respectively. A schematic of a BDFM-based wind turbine drivetrain is illustrated in Fig. 1.

The BDFM structure and operations are more complex than conventional DFIGs, and they require extensive analysis. Different BDFM analytical models have been developed to aid the understanding of the operations of BDFMs, and for design-related objectives [1]. The coupled circuit (CC) modelling has been commonly used in developing non-salient pole electric machine models, and is a relatively easy to understand the approach to machine modelling. From the CC viewpoint, a machine is modelled as an electric circuit with variable inductances dependent on the rotor position [6]. The flux linkages and magnetic field co-energy in a CC are based on currents and inductances. Furthermore, the CC approach has been utilised to develop BDFM models in [7–11] with reasonably accurate results, and have provided useful insight about BDFM operations.

The CC BDFM model in [7] is developed for BDFMs with cage +NL rotors in pumped storage hydro generation and regenerative traction applications. Steady-state and dynamic operations are investigated for the machine in the simple induction mode and during no load acceleration. The simulation results of the CC model introduced in [7] are compared with experimental results in [8]. The response of the motor in the synchronous doubly fed mode to increasing the load torque till the loss of synchronism is also illustrated in terms of the PW currents and the motor speed. It should be noted that the stator of the BDFM in [7, 8] consists of ninre similarly wound coil groups arranged in three Y-connected sets supplied by two independent three-phase supplies. Also, only the CC model results are illustrated for the synchronous motoring mode.

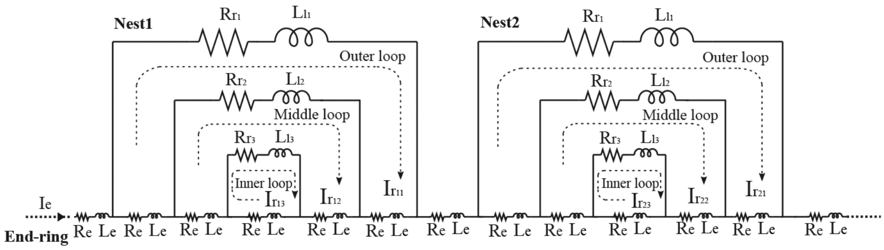

Fig. 2 *Circuit model of NL rotor*

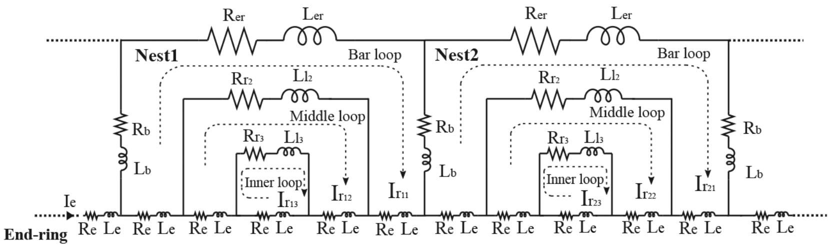

Fig. 3 *Circuit model of cage+NL rotor*

The CC BDFM model in [9] builds on the model described in [7, 8]. The CC is transformed to the *dq*-axis in the synchronous reference frame. Only the NL rotor is considered in [9], and a model reduction procedure is performed to represent the rotor as a single *dq* pair. The model in [9] is ultimately developed for simplification of BDFM controllers.

The CC models in [10, 11] are developed for dual-stator winding induction machines. Although the dual-stator winding induction machine is differentiated from the contemporary BDFM in [10, 11], the structures and operations of both machine types have similarities. The models in [10, 11] are predominantly focused on wide speed range motoring operations. Also, the machine rotor in [10, 11] is the standard squirrel cage rotor, which is not ideal for BDFMs. The machine inductances are calculated using the winding function theory (WFT) in [11].

The WFT, described in [12], uses details about the machine geometry and the physical arrangement of the windings to calculate the MMF per unit current in the windings. The MMFs are used to calculate flux linkages in the windings, from which the self and mutual inductances are calculated. The WFT is used in [13] in the modelling of non-sinusoidally wound induction machines for steady-state and dynamic simulations, and in [14], it is used in the dynamic analysis of induction machines with stator, rotor bars and end ring faults. In [15], the WFT is also used in the evaluation of the rotor bar and end ring currents of multiphase induction machines.

In [16], different loops with varying loop spans are combined to configure a number of NL rotor constructions. These rotors are simulated using finite element analysis (FEA) to investigate the contributions of NL rotor loops to torque production and total harmonic distortion. It was observed that the outer loops contributed more to the torque, and the determined the overall harmonic distortion. Suggestions for further investigation of the contributions of the loops to torque ripple were also raised.

In this paper, the WFT is used to calculate inductances in the development of a CC model for BDFMs with NL and cage+NL rotors. BDFMs with NL and cage+NL rotors designed for the 160L induction machine frames are simulated using the developed CC model. Instead of solely examining motoring operations like in [7, 8, 10, 11], synchronous doubly fed generating conditions are investigated extensively. The CC model simulation results are compared with FEA simulation results of the same machines.

Different simulation results are used to illustrate preliminary design applications of the CC model, and to provide insight into the operations of BDFMs. The effect of the rotor loop spans on the BDFM stator to rotor mutual inductances are discussed, and used to illustrate the torque contributions of the BDFM rotors loops. The effect of rotor loops on BDFM torque ripple is also investigated, and potential ways of mitigating the torque ripple by proper selection of rotor type and/or a number of rotor loops are discussed and illustrated. The CC model is also used to provide a quick and robust method for determining the BDFM rotor currents at different operating conditions.

2 Coupled circuit model

The following assumptions are made in the modelling of BDFMs:

- The effects of saturation are neglected.
- The air gap of the BDFM is uniform, and there is no rotor eccentricity.
- $p_1 \neq p_2$, therefore, there is no direct coupling between the PW and the CW.
- Voltage excitations are considered at the PW, while current excitations are considered at the CW.

2.1 Stator voltage and current equations

The three- phase PW voltage vector ($\boldsymbol{V_p}$) can be represented as

$$\boldsymbol{V_p} = [V_{p_1}\ V_{p_2}\ V_{p_3}]^{\mathrm{t}}. \tag{1}$$

Using general winding voltage equations as used in [11, 13], $\boldsymbol{V_p}$ can be calculated as follows:

$$\boldsymbol{V_p} = \boldsymbol{R_p I_p} + \frac{\mathrm{d}t\boldsymbol{\lambda_p}}{\mathrm{d}t}, \tag{2}$$

where $\boldsymbol{R_p}$ is the PW resistance matrix, $\boldsymbol{I_p}$ is the PW current vector, and $\boldsymbol{\lambda_p}$ is the PW flux linkage matrix. $\boldsymbol{R_p}$ is given as

$$\boldsymbol{R_p} = r_p \boldsymbol{I}, \tag{3}$$

where r_p is the PW phase winding resistance and $\boldsymbol{I}$ is a 3×3 identity matrix. The PW current vector ($\boldsymbol{I_p}$) is represented as

$$\boldsymbol{I_p} = [I_{p_1}\ I_{p_2}\ I_{p_3}]^{\mathrm{t}}. \tag{4}$$

$\boldsymbol{\lambda_p}$ is then calculated as

$$\boldsymbol{\lambda_p} = \boldsymbol{L_p I_p} + \boldsymbol{L_{pr} I_r}, \tag{5}$$

where $\boldsymbol{L_p}$ is the PW inductance matrix, $\boldsymbol{L_{pr}}$ is the instantaneous mutual inductance matrix between the PW and the rotor windings (loops), and $\boldsymbol{I_r}$ illustrated in Figs. 2 and 3, see the Appendix is the rotor loops current vector. $\boldsymbol{L_p}$ can be written as

$$\boldsymbol{L_p} = \begin{bmatrix} L_{p_{11}} & L_{p_{12}} & L_{p_{13}} \\ L_{p_{21}} & L_{p_{22}} & L_{p_{23}} \\ L_{p_{31}} & L_{p_{32}} & L_{p_{33}} \end{bmatrix}. \tag{6}$$

With $\boldsymbol{V_p}$ being the grid voltage, the PW flux linkages, $\boldsymbol{\lambda_p}$, can also be calculated from (2) as

$$\boldsymbol{\lambda_p} = \int (\boldsymbol{V_p} - \boldsymbol{R_p I_p})\mathrm{d}t. \tag{7}$$

The PW current ($\boldsymbol{I_p}$) is then calculated from (5) as

$$\boldsymbol{I_p} = \boldsymbol{L_p^{-1} \lambda_p} - \boldsymbol{L_p^{-1} L_{pr} I_r}. \tag{8}$$

2.2 Rotor voltage and current equations

The rotor loops voltage vector ($\boldsymbol{V_r}$) obtained by mesh analysis of the loops is given by

$$\boldsymbol{V_r} = \boldsymbol{R_r I_r} + \frac{\mathrm{d}\boldsymbol{\lambda_r}}{\mathrm{d}t}, \tag{9}$$

where $\boldsymbol{R_r}$ is the rotor loops resistance matrix illustrated in (31) and (32) (see the Appendix) for the NL and cage+NL rotors, respectively, $\boldsymbol{I_r}$ is the rotor loops current vector and $\boldsymbol{\lambda_r}$ is the rotor loops flux linkage vector. $\boldsymbol{I_r}$ can be represented as

$$\boldsymbol{I_r} = [I_{r_{11}}\, I_{r_{12}}\, I_{r_{13}}\, I_{r_{21}}\, .\ .\ I_{r_{ni}}\, .\ .\ I_e]^{\mathrm{t}}, \tag{10}$$

where $I_{r_{ni}}$ is the current in the ith loop of a rotor nest n and I_{e} is the end ring current. $\boldsymbol{\lambda_r}$ can be calculated as

$$\boldsymbol{\lambda_r} = \boldsymbol{L_r I_r} + \boldsymbol{L_{pr}^t I_p} + \boldsymbol{L_{cr}^t I_c}, \tag{11}$$

where $\boldsymbol{L_r}$ is the rotor loops inductance matrix illustrated in (33) and (34) (see the Appendix) for the NL and cage+NL rotors, respectively. $\boldsymbol{L_{pr}^{\mathrm{t}}}$ is the instantaneous mutual inductance between the PW and the rotor loops matrix transpose, while $\boldsymbol{L_{cr}^{\mathrm{t}}}$ is the instantaneous mutual inductance between the CW and the rotor loops matrix transpose.

The lower end ring short circuits the loops in both rotor types, effectively making all elements of $\boldsymbol{V_r}$ equal to zero at any time instance. Thus, (9) can be modified to calculate $\boldsymbol{\lambda_r}$ as

$$\boldsymbol{\lambda_r} = -\int \boldsymbol{R_r I_r}\mathrm{d}t. \tag{12}$$

$\boldsymbol{I_r}$ can then be calculated from (11) as

$$\boldsymbol{I_r} = \boldsymbol{L_r^{-1}} \lambda_r - \boldsymbol{L_r^{-1} L_{pr}^{\mathrm{t}} I_p} - \boldsymbol{L_r^{-1} L_{cr}^{\mathrm{t}} I_c}. \tag{13}$$

The instantaneous mutual inductance matrix between the PW and the rotor loops ($\boldsymbol{L_{pr}}$) is represented as

$$\boldsymbol{L_{pr}} = \begin{bmatrix} L_{p_1 r_{11}} & L_{p_1 r_{12}} & \cdots & L_{p_1 r_{ni}} \\ L_{p_2 r_{11}} & L_{p_2 r_{12}} & \cdots & L_{p_2 r_{ni}} \\ L_{p_3 r_{11}} & L_{p_3 r_{12}} & \cdots & L_{p_3 r_{ni}} \end{bmatrix}, \tag{14}$$

where $L_{p_m r_{ni}}$ is the instantaneous mutual inductance between PW winding m and a rotor loop i in a nest n. The instantaneous mutual inductance matrix between the CW and the rotor loops, $\boldsymbol{L_{cr}}$, is represented as

$$\boldsymbol{L_{cr}} = \begin{bmatrix} L_{c_1 r_{11}} & L_{c_1 r_{12}} & \cdots & L_{c_1 r_{ni}} \\ L_{c_2 r_{11}} & L_{c_2 r_{12}} & \cdots & L_{c_2 r_{ni}} \\ L_{c_3 r_{11}} & L_{c_3 r_{12}} & \cdots & L_{c_3 r_{ni}} \end{bmatrix}. \tag{15}$$

where $L_{c_m r_{ni}}$ is the instantaneous mutual inductance between CW winding m and a rotor loop i in a nest n.

2.3 Torque equation

Considering BDFMs as linear magnetic systems, the electromagnetic torque (T_{e}) can be obtained from the partial derivative of the co-energy with respect to the rotor position. Similar to [10, 11], T_{e} is calculated as

$$T_{\mathrm{e}} = \begin{bmatrix} \boldsymbol{I_p^{\mathrm{t}}} & \boldsymbol{I_c^{\mathrm{t}}} \end{bmatrix} \begin{bmatrix} \dfrac{\mathrm{d}\boldsymbol{L_{pr}}}{\mathrm{d}\theta} \\ \dfrac{\mathrm{d}\boldsymbol{L_{cr}}}{\mathrm{d}\theta} \end{bmatrix} \boldsymbol{I_r}, \tag{16}$$

where $\boldsymbol{I_c}$ is the CW current vector represented as

$$\boldsymbol{I_c} = \begin{bmatrix} I_{c_1} & I_{c_2} & I_{c_3} \end{bmatrix}^{\mathrm{t}}. \tag{17}$$

$(\mathrm{d}\boldsymbol{L_{pr}}/\mathrm{d}\theta)$ is the matrix of the change in mutual inductances between the PW and the rotor loops with changes in position, and $(\mathrm{d}\boldsymbol{L_{cr}}/\mathrm{d}\theta)$ is the matrix of the change in mutual inductances between the CW and the rotor loops with changes in the position.

2.4 Inductance calculation using the WFT

The winding function (WF), $N(\theta)$, of a machine winding is the MMF distribution of that winding for a current of 1 A [12]. The WF can be calculated as

$$N(\theta) = n(\theta) - \langle n(\theta) \rangle, \tag{18}$$

where $n(\theta)$ is the turns function and $\langle n(\theta) \rangle$ is the average value of the turns function along the core periphery. The turns function is the number of series turns (N) enclosed in the winding [12]. The average turns function ($\langle n(\theta) \rangle$) can be calculated as

$$\langle n(\theta) \rangle = \frac{1}{2\pi} \int_0^{2\pi} n(\theta)\mathrm{d}\theta. \tag{19}$$

Single-layer phase windings with p pole pairs can be considered as consisting of q concentrated full pitch coils, where q is the number of slots per pole per phase. These concentrated coils with N number of series turns (equal to the number of turns in the slot) are displaced by $(\pi/(3pq))$ for three-phase windings. The phase WF can then be obtained by adding the WFs of these concentrated coils together. In Fig. 4, the WF of an arbitrary phase winding with p pole pairs and $q = 3$, is illustrated by combining WFs of three concentrated full pitch coils. It should be noted that in Fig. 4, n_c is the number of turns in a slot.

The magnetising inductance of phase winding a (L_{aa}) is calculated using its WF ($N_a(\theta)$) as

$$L_{aa} = \frac{\mu_0 r l}{g} \int_0^{2\pi} N_a^2(\theta)\mathrm{d}\theta, \tag{20}$$

where μ_0 is the permeability of free space, r is the machine airgap radius, and l is the machine stack length [12]. The mutual inductance between phase winding a and another phase winding b (L_{ab}) is calculated as

$$L_{ab} = \frac{\mu_0 r l}{g} \int_0^{2\pi} N_a(\theta) N_b(\theta)\mathrm{d}\theta. \tag{21}$$

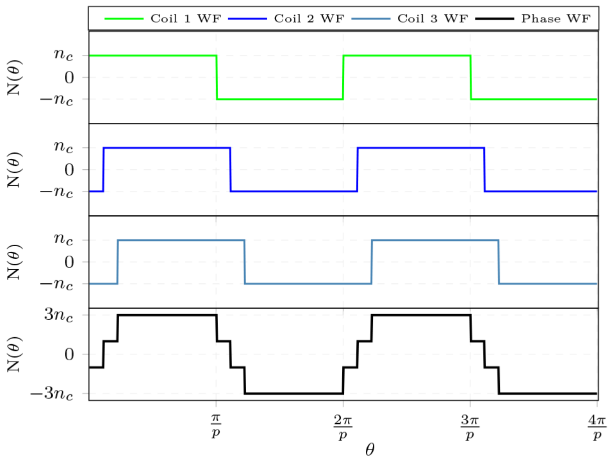

Fig. 4 *Combination of the WFs of three concentrated full pitch coils to form the WF of a phase winding with p pole pairs and q = 3*

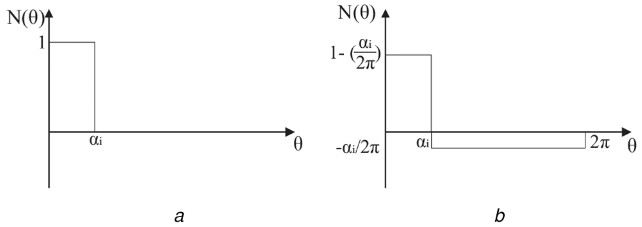

Fig. 5 *Winding illustration of rotor loop i*
(a) Turns function, ***(b)*** WF

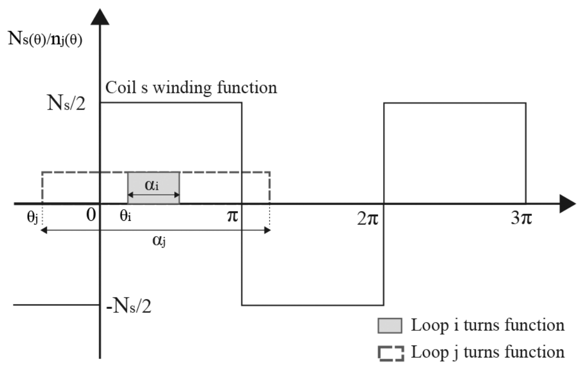

Fig. 6 *Rotor loop turn functions in relation to a concentrated stator coil winding function*

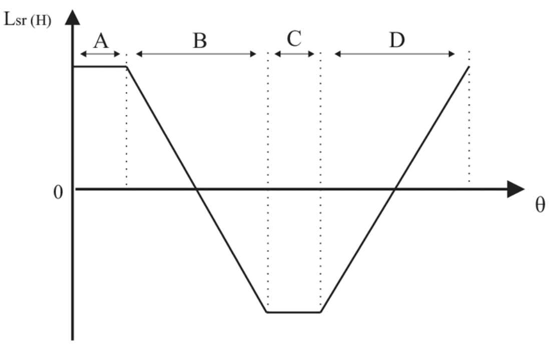

Fig. 7 *Mutual inductance between a concentrated stator coil and a rotor loop*

2.5 NL rotor inductance calculations using the WFT

The turns function and WF of a rotor loop are illustrated in Fig. 5. The number of series turns for a NL made of bars is 1, and the magnetising inductance of an arbitrary rotor loop i, $L_{r_{ii}}$, is

$$L_{r_{ii}} = \frac{\mu_0 rl}{g}\alpha_i\left(1 - \frac{\alpha_i}{2\pi}\right), \tag{22}$$

where α_i is the angular loop span of loop i [13]. The mutual inductance, $L_{r_{ni,nj}}$, between two rotor loops i and j in the same nest n, with loop spans α_i and α_j, respectively, is calculated as

$$L_{r_{ni,nj}} = \frac{\mu_0 rl}{g}\alpha_j\left(1 - \frac{\alpha_i}{2\pi}\right), \tag{23}$$

where $\alpha_i > \alpha_j$. For loops in different nests, e.g. loop i in nest n and loop j in nest k, with loop spans α_i and α_j, respectively, the mutual inductance $L_{r_{ni,kj}}$ is

$$L_{r_{ni,kj}} = \frac{\mu_0 rl}{g}\left(\frac{-\alpha_i\alpha_j}{2\pi}\right). \tag{24}$$

2.6 Mutual inductance between stator and rotor windings calculation using WFT

For convenience, the mutual inductances between a stator winding and rotor loops are first described using a full pitch, two-pole, concentrated stator coil. The positioning of two rotor loops i and j with different loop spans relative to the concentrated stator coil s with N_s series turns is illustrated in Fig. 6. Loop i has a loop span, α_i, which is less than the pole span of the coil s, while loop j has loop span, α_j, which is greater than the pole span of coil s. In general, most loops in BDFM rotors are like loop i, with loop spans less than either the PW or the CW pole spans. However, the loops formed by the $(p_1 + p_2)$ cage bars in the cage+NL rotor are generally longer than the CW pole span, hence the consideration of loop type j.

The instantaneous mutual inductance L_{sr_k} between coil s and any rotor loop k regardless of loop span is given as

$$L_{sr_k} = \frac{\mu_0 rl}{g}\int_0^{2\pi} N_s(\theta)N_k(\theta)\mathrm{d}\theta, \tag{25}$$

where $N_s(\theta)$ is the WF of coil s and $N_k(\theta)$ is the WF of rotor loop k. Four distinct regions in the calculation of the mutual inductance (L_{sr}) between the two-pole concentrated stator coil s and the rotor loops are illustrated in Fig. 7. It should be noted that the left-hand side of the rotor turns functions is taken as the reference point for θ.

The mutual inductance between coil s and rotor loop type i $\left(L_{sr_i}\right)$ in these regions is calculated as

$$\begin{aligned}
&\text{A}. \quad L_{sr_i} = \frac{\mu_0 rl}{g}\frac{N_s}{2}\alpha_i, && 0 \le \theta_i \le \pi - \alpha_i\,.\\
&\text{B}. \quad L_{sr_i} = \frac{\mu_0 rl}{g}\frac{N_s}{2}(2\pi - 2\theta_i - \alpha_i), && \pi - \alpha_i < \theta_i \le \pi\,.\\
&\text{C}. \quad L_{sr_i} = -\frac{\mu_0 rl}{g}\frac{N_s}{2}\alpha_i, && \pi < \theta_i \le 2\pi - \alpha_i\,.\\
&\text{D}. \quad L_{sr_i} = \frac{-\mu_0 rl}{g}\frac{N_s}{2}(4\pi - 2\theta_i - \alpha_i), && 2\pi - \alpha_i < \theta_i \le 2\pi\,.
\end{aligned} \tag{26}$$

The mutual inductance between coil s and rotor loop type j $\left(L_{sr_j}\right)$ in these regions is calculated as

$$\begin{aligned}
&\text{A}. \quad L_{sr_j} = \frac{\mu_0 rl}{g}\frac{N_s}{2}(2\pi + \alpha_j), && \theta_j \le 0, \theta_j + \alpha_j \ge \pi\,.\\
&\text{B}. \quad L_{sr_j} = \frac{\mu_0 rl}{g}\frac{N_s}{2}(2\pi - 2\theta_j - \alpha_j), && \theta_j > 0, \theta_j + \alpha_j < 2\pi\\
&\text{C}. \quad L_{sr_j} = -\frac{\mu_0 rl}{g}\frac{N_s}{2}(2\pi + \alpha_j), && \theta_j \le \pi, \theta_j + \alpha_j \ge 2\pi\\
&\text{D}. \quad L_{sr_j} = -\frac{\mu_0 rl}{g}\frac{N_s}{2}(4\pi - 2\theta_j - \alpha_j), && \theta_j > \pi, \theta_j + \alpha_j < 3\pi
\end{aligned} \tag{27}$$

Table 1 160L frame BDFM design specifications

Item	Symbol	Unit	Value
grid voltage, rms	V_p	V	230
PW frequency	f	Hz	50
rated slip	—	—	−0.35
PW current, rms	I_p	A	4.77
CW current, rms	I_c	A	3.16
PW pole pairs	p_1	—	2
CW pole pairs	p_2	—	3
natural speed	ω_n	rpm	600
airgap length	g	mm	0.35
stack length	l	mm	240
airgap radius	r	mm	85.5
stator slots	n_s	—	36
PW turns per phase	N_{pw}	—	234
CW turns per phase	N_{cw}	—	432
NL rotor slots	n_{r1}	—	30
cage+NL rotor slots	n_{r2}	—	25

The change in mutual inductance between coil s and loop type i with respect to position $((\mathrm{d}Lsr_i)/(\mathrm{d}\theta_i))$ is calculated in the four regions as

$$\begin{aligned} &\mathrm{A.}\quad \frac{\mathrm{d}L_{sr_i}}{\mathrm{d}\theta_i} = 0, && 0 \le \theta_i \le \pi - \alpha_i\,. \\ &\mathrm{B.}\quad \frac{\mathrm{d}L_{sr_i}}{\mathrm{d}\theta_i} = \frac{-2\mu_0 rl}{g}\frac{N_s}{2}, && \pi - \alpha_i < \theta_i \le \pi\,. \\ &\mathrm{C.}\quad \frac{\mathrm{d}L_{sr_i}}{\mathrm{d}\theta_i} = 0, && \pi < \theta_i \le 2\pi - \alpha_i\,. \\ &\mathrm{D.}\quad \frac{\mathrm{d}L_{sr_i}}{\mathrm{d}\theta_i} = \frac{2\mu_0 rl}{g}\frac{N_s}{2}, && 2\pi - \alpha_i < \theta_i \le 2\pi\,. \end{aligned} \tag{28}$$

The change in mutual inductance between coil s and loop type j with respect to position $((\mathrm{d}Lsr_j)/(\mathrm{d}\theta_j))$ is calculated in the four regions as

$$\begin{aligned} &\mathrm{A.}\quad \frac{\mathrm{d}L_{sr_j}}{\mathrm{d}\theta_j} = 0, && \theta_j \le 0, \theta_j + \alpha_j \ge \pi\,. \\ &\mathrm{B.}\quad \frac{\mathrm{d}L_{sr_j}}{\mathrm{d}\theta_j} = -\frac{2\mu_0 rl}{g}\frac{N_s}{2}, && \theta_j > 0, \theta_j + \alpha_j < 2\pi\,. \\ &\mathrm{C.}\quad \frac{\mathrm{d}L_{sr_j}}{\mathrm{d}\theta_j} = 0, && \theta_j \le \pi, \theta_j + \alpha_j \ge 2\pi\,. \\ &\mathrm{D.}\quad \frac{\mathrm{d}L_{sr_j}}{\mathrm{d}\theta_j} = \frac{2\mu_0 rl}{g}\frac{N_s}{2}, && \theta_j > \pi, \theta_j + \alpha_j < 3\pi\,. \end{aligned} \tag{29}$$

Generally, distributed phase windings with p pole pairs >1 are used in BDFM stators. In applying (26)–(29), the $Ns/2$ term becomes $Ns/2p$. It should also be noted that θ is the mechanical angle. Coils with higher p pole pairs will have smaller pole spans, such that during one complete mechanical revolution, there will be p repetitions of the regions in (26)–(29).

It should be recalled that the stator phase windings can be broken down into a group of q concentrated coils displaced by a stator slot pitch. These concentrated coils WFs can be used in calculating the mutual inductances between a stator phase winding and a rotor loop.

3 Simulation results and discussion

The CC model is developed using MATLAB scripts, and two BDFMs sized for a 160L induction machine frame (with identical stator windings) are simulated. One BDFM has an NL rotor, and the other, a cage+NL rotor. The specifications of the BDFMs are given in Table 1. Three rotor loops per nest are initially considered because of the machine ratings and following trends in the literature like [4, 9, 17]. Rotors with more loops per nest are considered later.

A flowchart summarising the CC model simulation and highlighting the relevant equations at each step is illustrated in Fig. 8. The WFs of the PW and CW are first obtained. The PW inductances, L_p, are calculated using the PW WFs, while the PW resistances, R_p, are calculated using the stator resistance formula in [18]. Initial simulation conditions such as the initial rotor position, load angle etc. are set and a time function is initialised. The instantaneous stator excitations are calculated together with the stator to rotor mutual inductances. The first set of simulation output is the rotor loop currents and flux linkages. These are used to calculate the PW flux linkages and currents from which the machine torque is then calculated.

2D time-stepping FEA simulations of the two BDFMs are compared with the CC model simulations. The FEA models are developed in ANSYS Maxwell®. An axial cross-section of a 2D FEA model of the BDFM with an NL rotor is illustrated in Fig. 9. The full model has to be simulated because of the lack of symmetry in the machine, leading to lengthy simulations. The flux lines in Fig. 9 demonstrate the $p_1 + p_2$ (5 in this case) rotating machine pole pairs. The PW occupies the bottom layer of the stator in the FEA model, while the CW occupies the top layer. The FEA models' rotor windings are developed using external circuits in ANSYS Maxwell®. Each rotor loop is designated as a winding connected to its calculated resistances and end connection leakage similar to Fig. 2. However, the bars in the cage+NL rotor are designated as individual windings with resistances to enable parallel connections like in Fig. 3. The M400-50A steel lamination type is used for all the BDFM FEA models with non-linearity of the core B–H curve considered.

The (CC and FEA) model PWs are excited with three-phase voltage excitations, while the CWs are excited with three-phase current excitations which have load angles relative to the PW voltage excitations. The instantaneous three-phase CW currents ($\boldsymbol{I_c}$) are calculated as

$$\begin{aligned} I_{c_1} &= \hat{I}_c \sin(2\pi f_2 t - \varphi_1), \\ I_{c_2} &= \hat{I}_c \sin\left(2\pi f_2 t - \frac{2\pi}{3} - \varphi_1\right), \\ I_{c_3} &= \hat{I}_c \sin\left(2\pi f_2 t + \frac{2\pi}{3} - \varphi_1\right), \end{aligned} \tag{30}$$

where $\hat{I}_c$ is the peak value of the rated CW current and φ_1 is the load angle. All simulation results for the (CC and FEA) models are obtained at steady states.

3.1 Stator to rotor mutual inductances

The CC model mutual inductances between the stator windings (PW and CW) and rotor loops of the BDFM with NL rotor are illustrated in Fig. 10, while mutual inductances between the stator windings (PW and CW) and rotor loops of the BDFM with cage +NL rotor are illustrated in Fig. 11. At first glance, it appears that wider rotor loops lead to smaller flat tops with rounded/sinusoidal edges of the mutual inductance waveform. This is the case for rotor loops with loop spans less than the stator winding pole span like the outer loop in Fig. 10*a*, the cage bar loop in Fig. 11*a*, and the middle loop in Fig. 11*b*. For loops with spans greater than the stator pole spans (such as the bar loop compared to the CW in Fig. 11*b*), a further increase in loop span leads to an increase in the waveform flat top, as can be observed from (27).

The outer loop of the BDFM with an NL rotor has a loop span which is the same as the CW pole span. In this case, the winding slot distribution of the CW has no major effect on its mutual inductance with the outer loop's waveform. The CW then couples similar to a concentrated coil with the rotor outer loop, hence the similarity of the mutual inductance waveform illustrated in Fig. 10*b* with Fig. 7.

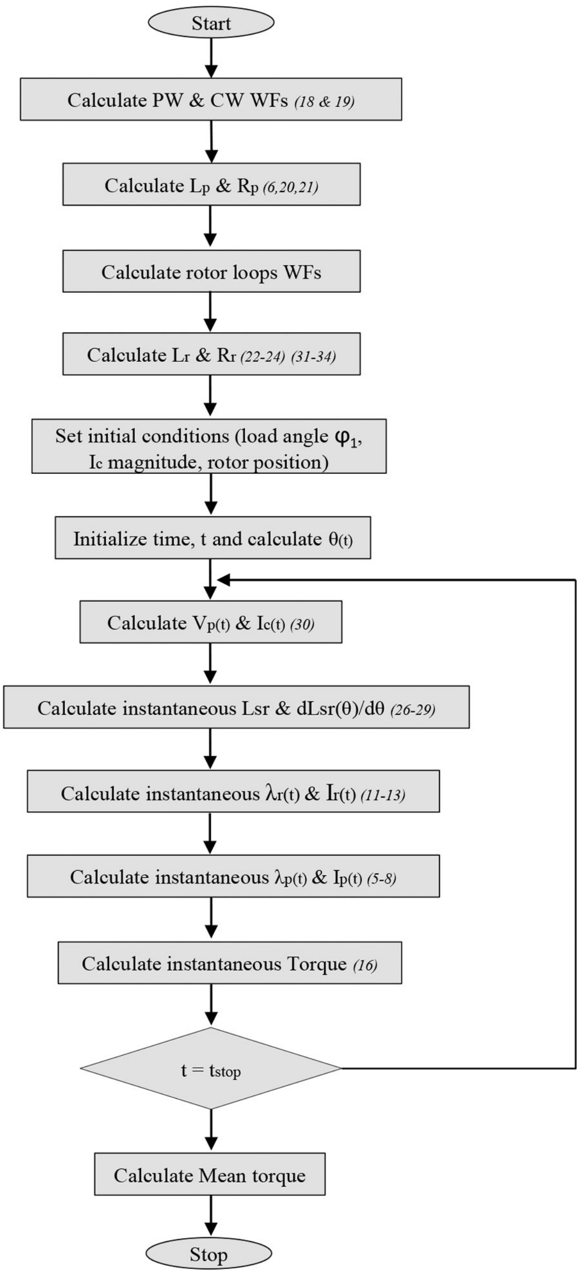

Fig. 8 *Flowchart of the CC model simulation in MATLAB®*

3.2 Electromagnetic torque

The mean torques at varying load angles for the BDFM with the NL rotor are illustrated for the different models at 0 and −0.35 slip in Figs. 12*a* and *b*, respectively. It should be noted that the load angles in Fig. 12 are used for illustration, and are not exact control-based angles. The mean torques at varying load angles for the BDFM with the cage+NL rotor are illustrated for the different models at 0 and −0.35 slip in Figs. 13*a* and *b*, respectively. The torque values of the CC models closely match those of the FEA models for both rotor types at 0 slip, with a slightly more noticeable variation at −0.35 slip.

The maximum generating torque achieved is higher than the maximum motoring torque for both BDFMs. Also, the BDFM with the cage+NL rotor produces slightly higher generating/motoring torque than the BDFM with the NL rotor for both CC and FEA models.

Using the CC model, the torque contributions of the rotor loops are investigated. This investigation is conducted using two sets of simulations. For the first set, different loops are removed from the rotors, and the total torques produced in the machines at varying load angle are illustrated in Figs. 14*a* and *b* for the NL and cage+NL rotors, respectively. It is observed that the removal of the outer loops leads to the highest drops in the torque production in both rotors. This suggests that the outer loops in both rotors have the largest contributions to torque production. This also corresponds with suggestions in [16] that wider loops contribute more to torque production.

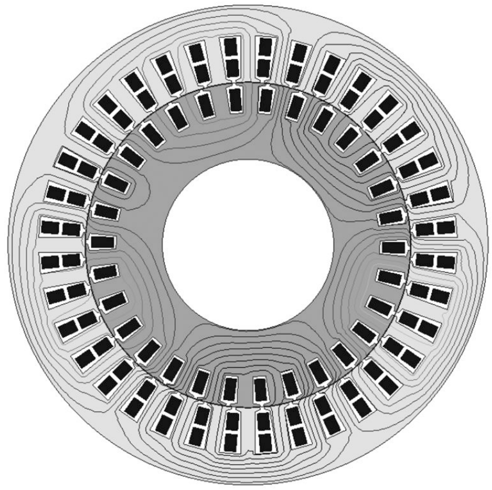

Fig. 9 *FEA model with flux lines of BDFM with an NL rotor*

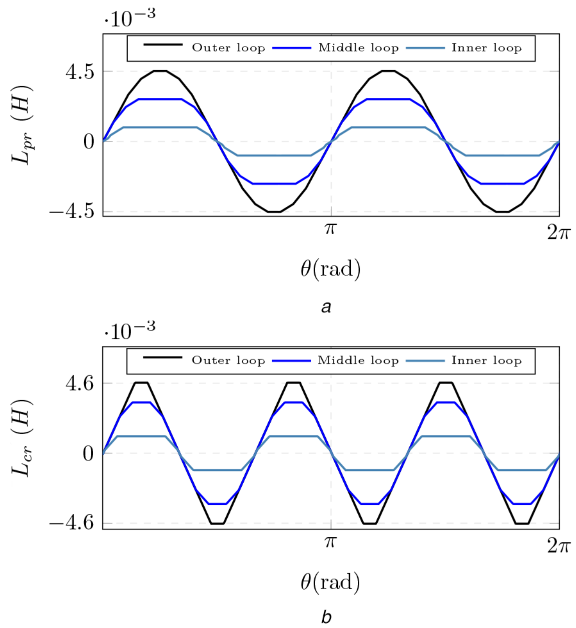

Fig. 10 *CC model mutual inductances between rotor loops in the NL rotor and*
(a) The PW, ***(b)*** The CW

However, the drop in torque production due to the removal of the outer loop in the cage+NL rotor in Fig. 14*b* is smaller than that of the outer loop of the NL rotor in Fig. 14*a*. The converse may have been expected as the outer loop of the cage+NL rotor is wider than the outer loop of the NL rotor.

To further investigate the loop contributions, the torque contributions of the loops at varying load angles are then separated without the removal of any loops using the CC models. These torque contributions of the loops at varying load angles are illustrated in Figs. 15*a* and *b* for the BDFMs with NL and cage+NL rotors, respectively. It should be noted that this type of separation is difficult to conduct using the FEA models.

The torque contributions of the loops of the BDFM with the NL rotor are straightforward; the wider the loop, the greater the torque contribution. However, for the BDFM with the cage+NL rotor, the outer loop does not provide the largest contribution to the torque as illustrated in Fig. 15*b*. The loss in torque contribution of the outer loops in the cage+NL rotor is attributed to the shared rotor bars of outer loops in adjacent nests.

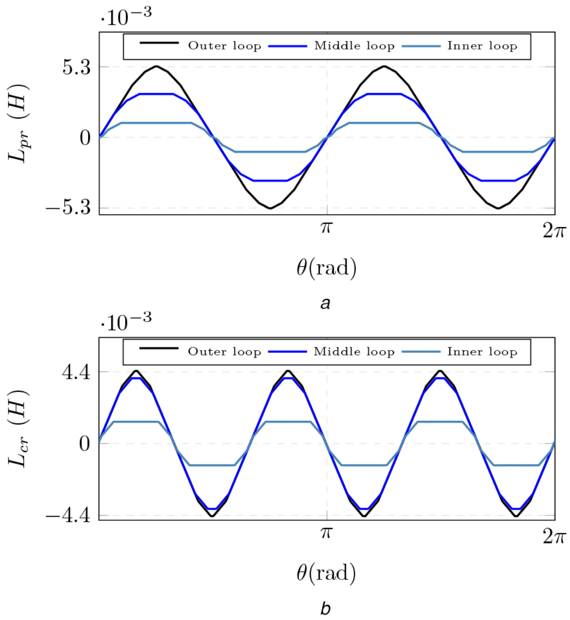

Fig. 11 *CC model mutual inductances between rotor loops in the cage +NL rotor and*
(a) The PW, ***(b)*** The CW

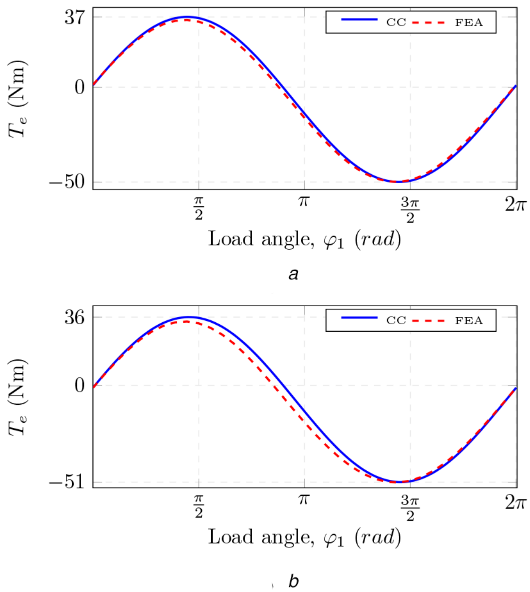

Fig. 12 *CC and FEA models mean torque at varying load angles of BDFM with the NL rotor at*
(a) 0 slip, ***(b)*** −0.35 slip

3.3 Torque ripple

Wind turbines are typically required by grid codes to run between 0.95 leading and lagging power factors [19]. Unity power factor condition falls in the middle of this range, and the torque ripple produced in the machines at generating unity power factor is investigated. Using the FEA and CC models, the torque produced at generating unity power factor conditions are illustrated in Figs. 16*a* and *b* for the BDFMs with the NL and cage+NL rotors, respectively.

The FEA models produce less torque ripple than the CC models for both rotor types, and this is likely due to the absence of slot effects in the CC models. Also, the difference in leakage calculations between the CC and FEA models are possible additional causes for the difference in ripple. Although the CC models produced greater ripple, both models for the BDFM with the cage+NL rotor produced less ripple than their corresponding models for the BDFM with the NL rotor. This illustrates the sensitivity of the CC models to the different rotor types. The

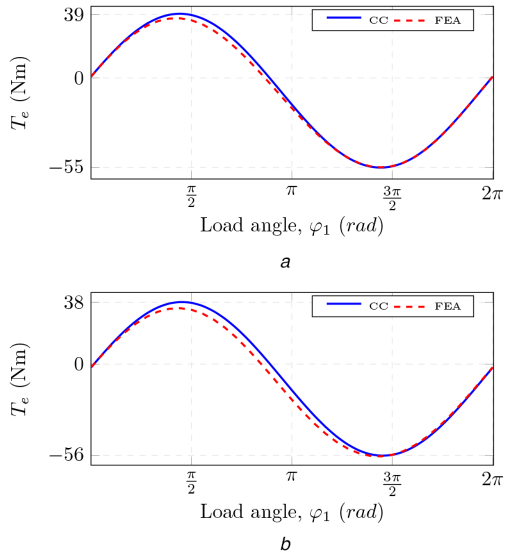

Fig. 13 *CC and FEA models mean torque at varying load angles of BDFM with the cage+NL rotor at*
(a) 0 slip, ***(b)*** −0.35 slip

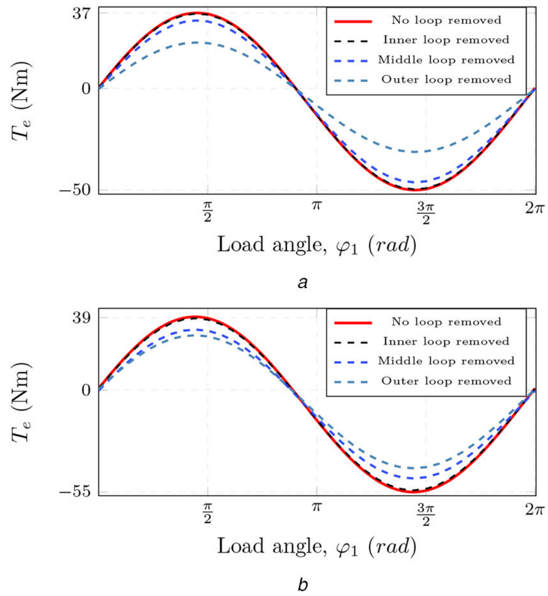

Fig. 14 *CC models mean torque at varying load angles with different rotor loops removed*
(a) NL rotor, ***(b)*** Cage+NL rotor

frequencies of torque oscillation are also the same for both model types.

Using the CC models, plots of the contributions of the different rotor loops to the unity power factor generating torque are illustrated in Figs. 17*a* and *b* for the BDFMs with the NL and cage +NL rotors, respectively. It is observed that the outer loops of both BDFMs produce the largest ripples. It should be recalled that the outer loop of the BDFM with the cage+NL rotor contributes less torque than the middle loop as illustrated in Fig. 15*b*, and also highlighted in Fig. 17*b*. Also, it can be observed that the loop torque ripples in the NL rotor are in step with each other, while the torque ripple of the outer loop of the cage+NL rotor is not in step with the ripples of the other loops. As a result, the torque ripples of the loops in an NL rotor add up, while the loop torque ripples in the cage+NL rotor have a more complex interaction.

Using the CC models, the torque contributions of the PW and CW at generating unity power factor are separately illustrated in Figs. 18*a* and *b* for the BDFMs with NL and cage+NL rotors, respectively. The PW torque contribution for both rotor types is closely matched in ripple and magnitude. However, the torque ripple produced by the CW in the BDFM with NL rotor is

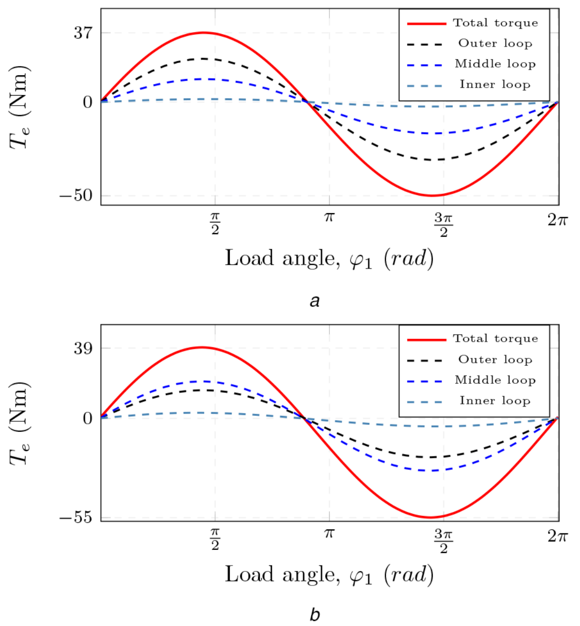

Fig. 15 *CC models loop torque contributions at varying load angles of BDFM with the*
(a) NL rotor, ***(b)*** Cage+NL rotor

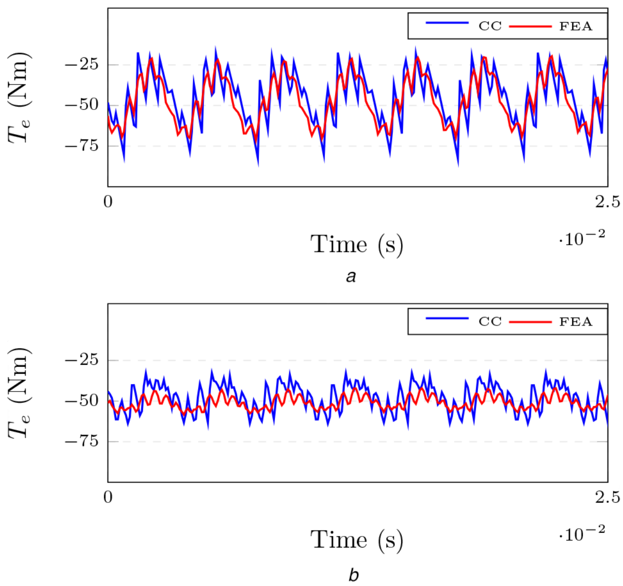

Fig. 16 *Generating unity power factor torque from CC and FEA models of BDFM with the*
(a) NL rotor, ***(b)*** Cage+NL rotor

significantly higher than the torque ripple produced by the CW in the BDFM with cage+NL rotor. Also, the CW contributes more torque in both BDFMs.

The reason for the higher torque ripple generated in the BDFM with the NL rotor can be explained using the mutual inductance between the CW and the outer loop of that particular NL rotor. Due to the peculiar situation where the CW pole span is equal to the NL rotor outer loop span, the effects of slot distribution are lost. The CW couples like a concentrated coil with the NL rotor outer loop, generating more harmonics, and consequently more torque ripple.

3.4 Stator and rotor currents

The FEA and CC models PW phase currents are illustrated in Figs. 19 and 20 for the BDFMs with the NL and cage+L rotors, respectively, at unity power factor generating conditions. The PW currents of both BDFMs with the different rotors and both models match closely. The loop currents of the BDFM with the NL rotor at peak generating torque are illustrated in Fig. 21 for the CC and

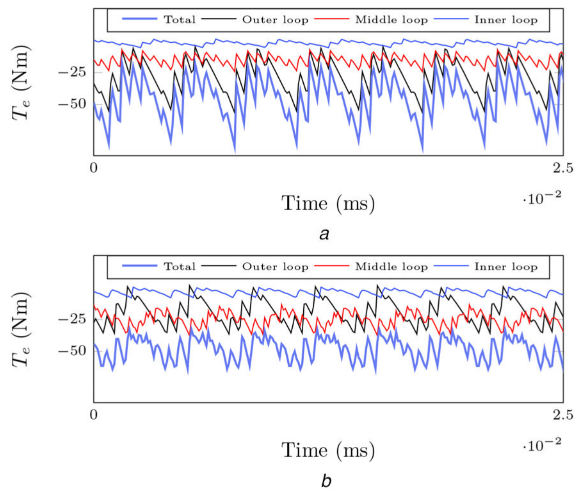

Fig. 17 *Rotor loops torque contributions using CC models of BDFM with the*
(a) NL rotor, ***(b)*** Cage+NL rotor

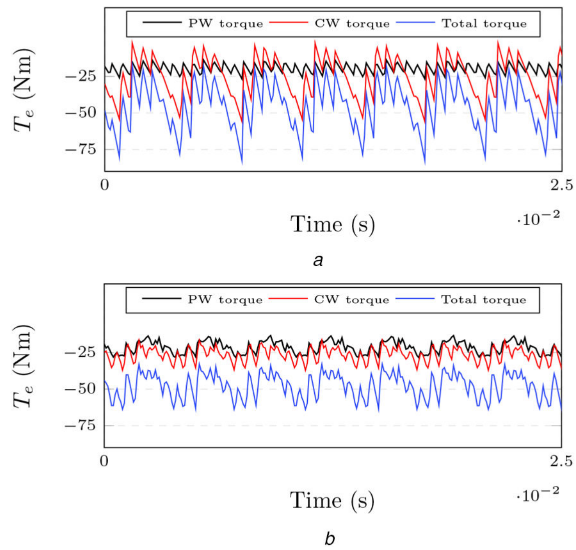

Fig. 18 *PW and CW torque contributions using CC models of BDFM with the*
(a) NL rotor, ***(b)*** Cage+NL rotor

FEA models, while those of the BDFM with the cage+NL rotor at generating unity power factor are illustrated in Fig. 22. It should be noted that the FEA model currents in Figs. 19–22 are shifted ahead slightly for clearer illustration.

The loop currents in the NL rotor for both models have similar waveforms and peak values. It can be observed that the loop currents in an NL rotor nest are all in phase, with the wider loops having higher current magnitudes.

Different windings cannot share coil-sides/bars in ANSYS Maxwell®. Thus, the cage+NL rotor outer loops (cage loops) cannot be modelled as windings, as done in the CC model. Instead, for the FEA model, the cage bars in the cage+NL rotor are modelled as individual windings and connected to the other loops using the external circuit, as mentioned in Section 3. As a result, the FEA bar currents are obtainable, but the outer loop currents are not. This is why only the CC model outer loop currents are illustrated in Fig. 22. The bar currents in the CC model are obtained by post-processing operations whereby adjacent outer loop currents are subtracted to obtain their shared bar currents.

The currents of the NLs in the cage+NL rotor are also in phase, and the current waveforms and peak values for both model types are similar. The illustrated bar currents lead the nested loop currents by approximately the rotor slot pitch. However, the combinations of adjacent bars which form the outer loops of the cage+NL rotor, cause the outer loop current to be in phase with

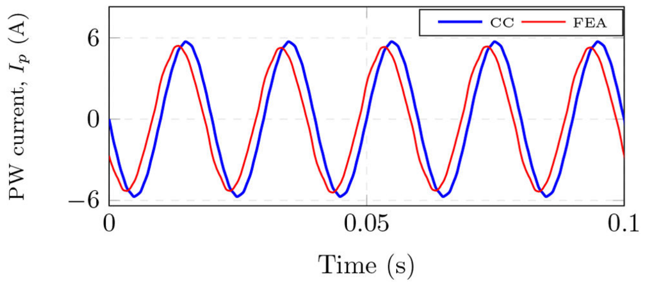

Fig. 19 *CC and FEA models PW phase current at generating unity power factor of BDFM with the NL rotor*

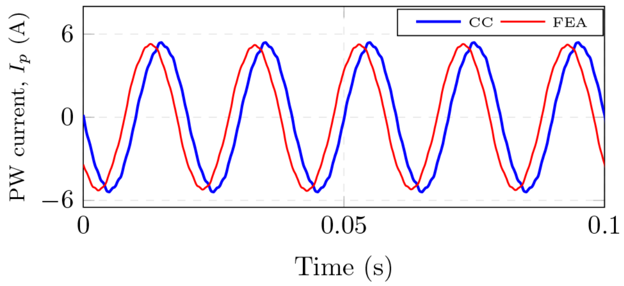

Fig. 20 *PW phase current from CC and FEA models at generating unity power factor of BDFM with the cage+NL rotor*

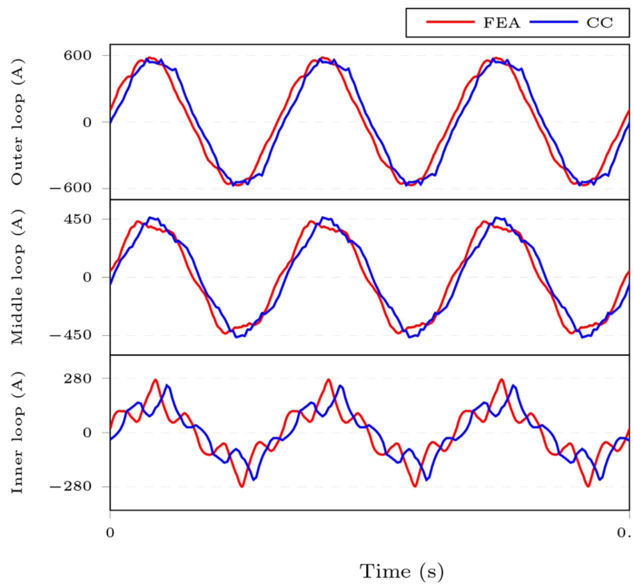

Fig. 21 *Rotor loop currents of BDFM with the NL rotor at peak generating torque*

nested loops in the same nest of the cage+NL rotor. It can be observed that the outer loop peak current is less than the middle loop peak current. This provides further understanding of why the torque contribution of the cage+NL rotor outer loop is lower than the middle loop contribution.

3.5 Effect of the number of stator slots and rotor loops in a nest

CC models are used to examine the effects of the number of nest loops on torque capabilities and ripple. As stated earlier, three loops per nest were initially selected for the BDFM rotors. Each rotor slot is assumed to be equidistant to adjacent slots. The torque produced at generating unity power factor in BDFMs designed for 160L frames with similar specifications given in Table 1, but a different number of rotor loops, are illustrated in Fig. 23*a*. The torque ripple produced in the machines is also illustrated in Fig. 23*b*.

It should be noted that a large number of loops may not always be practical depending on the machine rating/frame size. The highest torque for the BDFM with the NL rotor is obtained at three loops, and four loops for the BDFM with the cage+NL rotor, after which the torque reduces progressively with increasing loops.

There is a general decrease in torque ripple with increases in loops for both BDFMs with the different rotors. Although there is a decrease in torque ripple with an increasing number of loops in the NL rotor, it is observed that there are spikes in torque ripple for every loop per nest number which is a multiple of three.

A different pole pair combination ($p_1 = 2, p_2 = 4$) is used to compare the initial combination. To achieve some fairness in comparison, similar stator slot numbers are used. Seventy-two stator slots are the smallest possible number of stator slots that can work with both pole pair combinations. The generating unity power factor torques of BDFMs with the different pole pair combinations having a different number of loops are illustrated in Fig. 24*a*, while the torque ripple produced in the BDFMs are illustrated in Fig. 24*b*.

For the $p_1 = 2$ and $p_2 = 3$ combination, the 72 stator slots models have a similar torque production and ripple pattern with the 36 slot models. However, the 72 slot models achieve considerably less torque ripple than the 36 slot models.

The $p_1 = 2$ and $p_2 = 4$ pole pair combination achieves greater torque than the $p_1 = 2$ and $p_2 = 3$ combination, which is expected as they have lower speeds for the same power rating. However, the $p_1 = 2$ and $p_2 = 4$ models have considerably higher torque ripple than their $p_1 = 2$ and $p_2 = 3$ counterparts. The $p_1 = 2$ and $p_2 = 4$ BDFM with an NL rotor has spikes in torque ripple for every loops per nest number which is a multiple of three also. For both pole pair combinations, the BDFMs with the cage+NL rotors also have the highest torque.

The illustrated increase of rotor loops and consequent effects indicate relatively greater flexibility with BDFM rotor design as compared to DFIG rotors which have very specific number of slots based on the DFIG PW poles. Also, considering the natural speeds of the two-pole pair combinations used, higher stator slot numbers would have been required for DFIGs based on the number of poles required for the desired speeds.

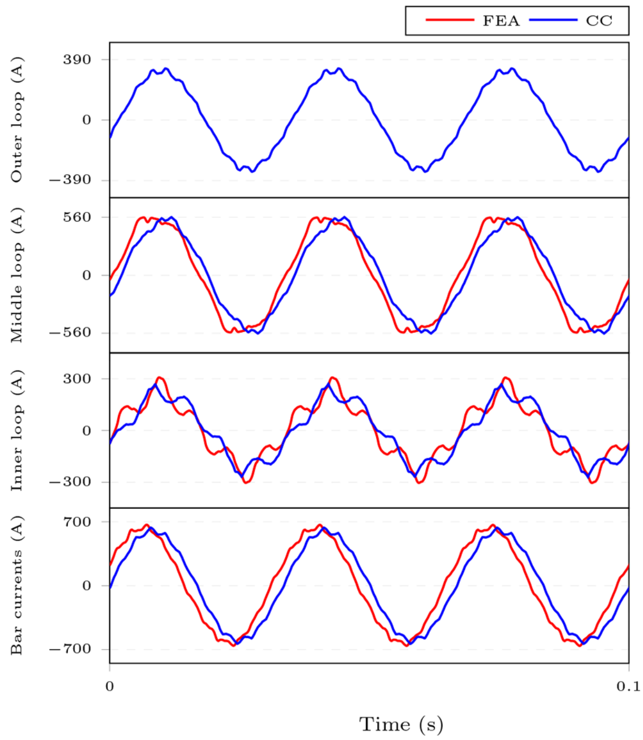

Fig. 22 *Rotor loop currents of BDFM with the cage+NL rotor at generating unity power factor*

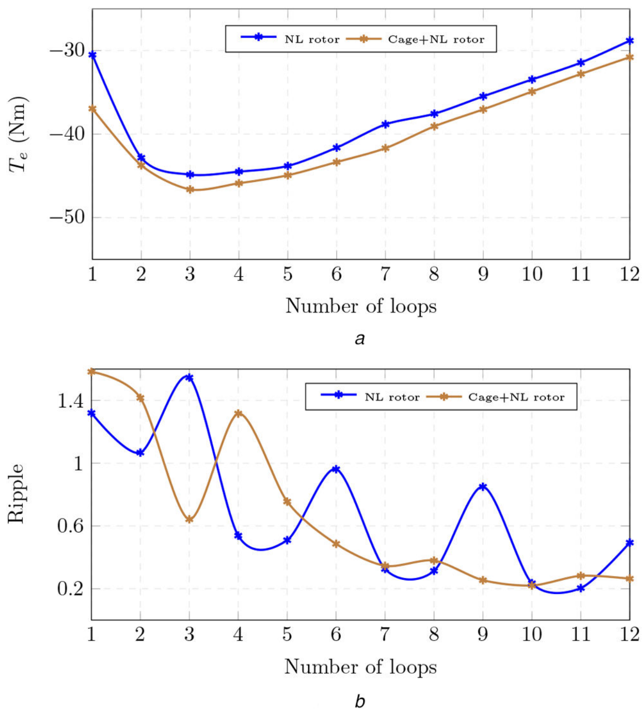

Fig. 23 *Effect of rotor loops on*
(a) Torque, ***(b)*** Torque ripple

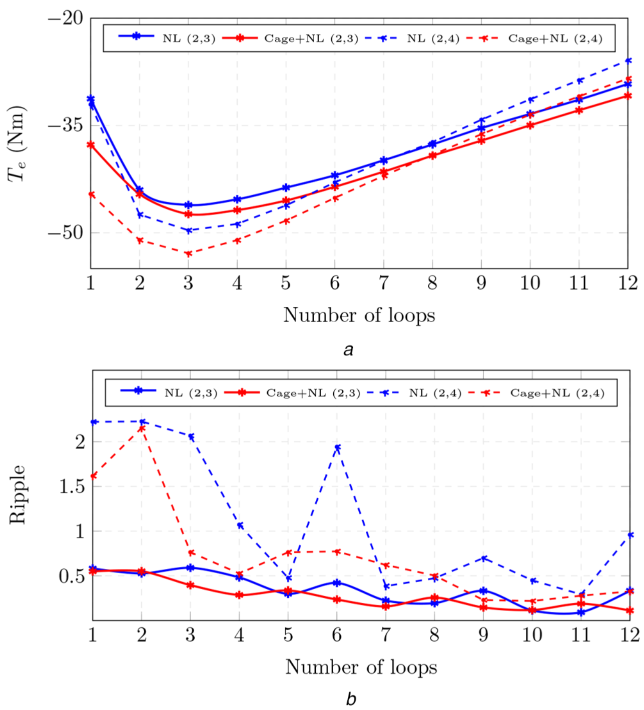

Fig. 24 *Effect of rotor loops in BDFMs with 72 stator slots on*
(a) Torque, ***(b)*** Torque ripple

4 Conclusion

CC models of BDFMs with NL and cage+NL rotors have been developed using the WFT, and the processes involved in the synchronous doubly fed mode have been illustrated. A revision of magnetising inductance calculations using the WFT was given, and the peculiar calculations of the BDFM rotor – rotor and stator – rotor mutual inductances have been outlined. The CC models mean torques at different load angles closely matched the FEA models mean torques. The CC models were also used to provide insight into the difference in torque magnitude and ripple between the BDFMs with NL and cage+NL rotors.

The CC models deliver considerable accuracy for use as a preliminary design tool for BDFMs. Before advanced design stages which require saturation investigations and optimisations, the CC models can be used to obtain useful design information, which would otherwise take considerably longer computation time using FEA models. An informed selection of rotor type and a number of loops can be conducted quickly by using the CC model with regard to desired power ratings and torque ripple. The torque and power factor of BDFMs change with varying load angle, and the power density of BDFMs within wind turbine power factor operating ranges can also be easily estimated using the CC models. The impact on torque capabilities of other factors such as the machine aspect ratio, stator slot numbers and pole pair combinations can also be estimated using the CC models. Further work can be done to incorporate the effects of slots and a saturation factor for even increased robustness.

5 References

[1] Strous, T.D., Polinder, H., Ferreira, J.A.: 'Brushless doubly-fed induction machines for wind turbines: developments and research challenges', *IET Electr. Power Appl.*, 2017, **11**, (6), pp. 991–1000

[2] Abdi, E., Tatlow, M.R., McMahon, R.A., *et al.*: 'Design and performance analysis of a 6 mw medium-speed brushless DFIG'. 2nd IET Renewable Power Generation Conf. (RPG 2013), Beijing, People's Republic of China, September 2013, pp. 1–4

[3] Carroll, J., McDonald, A., McMillan, D.: 'Reliability comparison of wind turbines with DFIG and PMG drive trains', *IEEE Trans. Energy Convers.*, 2015, **30**, (2), pp. 663–670

[4] Mcmahon, R., Tavner, P., Abdi, E., *et al.*: 'Characterising brushless doubly fed machine rotors', *IET Electr. Power Appl.*, 2013, **7**, (7), pp. 535–543

[5] Roberts, P.C.: 'A study of brushless doubly-fed (induction) machines'. PhD dissertation, University of Cambridge, September 2004

[6] Umans, S., Fitzgerald, A., Kingsley, C.: '*Electric machinery*' (McGraw-Hill Higher Education, New York, USA, 2013, 7th edn.)

[7] Wallace, A.K., Spee, R., Lauw, H.K.: 'Dynamic modeling of brushless doubly-fed machines'. Conf. Record of the IEEE Industry Applications Society Annual Meeting, vol.1, San Diego, CA, USA, October 1989, pp. 329–334

[8] Spee, R., Wallace, A.K., Lauw, H.K.: 'Performance simulation of brushless doubly-fed adjustable speed drives'. Conf. Record of the IEEE Industry Applications Society Annual Meeting, vol.1, San Diego, CA, USA, October 1989, pp. 738–743

[9] Roberts, P.C., Long, T., Mcmahon, R.A., *et al.*: 'Dynamic modelling of the brushless doubly fed machine', *IET Electr. Power Appl.*, 2013, **7**, (7), pp. 544–556

[10] Munoz, A.R., Lipo, T.A.: 'Dual stator winding induction machine drive', *IEEE Trans. Ind. Appl.*, 2000, **36**, (5), pp. 1369–1379

[11] Wu, Z., Ojo, O.: 'Coupled-circuit-model simulation and airgap-field calculation of a dual-stator-winding induction machine', *IEE Proc., Electr. Power Appl.*, 2006, **153**, (3), pp. 387–400

[12] Lipo, T.: '*Analysis of synchronous machines*' (CRC Press, Boca Raton, FL, USA, 2012)

[13] Toliyat, H.A., Lipo, T.A., White, J.C.: 'Analysis of a concentrated winding induction machine for adjustable speed drive applications. i. Motor analysis', *IEEE Trans. Energy Convers.*, 1991, **6**, (4), pp. 679–683

[14] Toliyat, H.A., Lipo, T.A.: 'Transient analysis of cage induction machines under stator, rotor bar and end ring faults', *IEEE Trans. Energy Convers.*, 1995, **10**, (2), pp. 241–247

[15] Gule, N., Kamper, M.J.: 'Evaluation of rotor bar and end ring current waveform of brush dc equivalent controlled multiphase cage rotor induction machine'. 2012 XXth Int. Conf. on Electrical Machines, Marseille, France, September 2012, pp. 946–952

[16] Wang, X., Liu, D., Polinder, H., *et al.*: 'Comparison of nested-loop rotors in brushless doubly-fed induction machines'. 2016 19th Int. Conf. on Electrical Machines and Systems (ICEMS), November 2016, pp. 1–6

[17] Gorginpour, H., Oraee, H., McMahon, R.: 'Performance description of brushless doubly-fed induction machine in its asynchronous and variable speed synchronous modes', *J. Electromagn. Anal. Appl.*, 2011, **3**, (12), pp. 490–511

[18] Boldea, I., Nasar, S.: '*The induction machines design handbook*' (Electric Power Engineering Series) (Taylor & Francis, Boca Raton, FL, USA, 2009, 2nd edn.)

[19] Tsili, M., Papathanassiou, S.: 'A review of grid code technical requirements for wind farms', *IET Renew. Power Gener.*, 2009, **3**, (3), pp. 308–332

6 Appendix

The circuit models of the NL and cage+NL rotors are illustrated in Figs. 2 and 3, respectively. The resistance matrix, $\boldsymbol{R_r}$, for the NL and cage+NL rotors is illustrated in (31) and (31), respectively, and the inductance matrix, $\boldsymbol{L_r}$, for the NL and cage+NL rotors is illustrated in (33) and (34), respectively.

R_{ri} is the ith resistance of a nested loop and it consists of the resistances of rotor bars from two slots and the loop overhang. R_e is the lower end ring segment resistance for both rotor types, while R_{er} is the cage upper end ring segment resistance for the cage+NL rotor, and n_r is the total number of rotor slots.

$L_{r_{ii}}$ is the magnetising inductance of any ith loop, while L_{l_i} is the total leakage inductance in any ith loop. The total leakage in the outer (bar) loops of the cage+NL rotors is $2L_{\mathrm{b}} + L_{\mathrm{er}} + 5L_{\mathrm{e}}$, where L_{b} is the rotor bar leakage inductance, L_{er} is the cage upper end ring segment leakage inductance, and L_e is the lower end ring segment leakage inductance. $L_{r_{ij}}$ is the mutual inductances between any loops i and loop j from the same nest, while $L_{r_{i,j}}$ is the mutual inductances between any loops i and loop j from different nests. Since similar loops in different nests have the same characteristics, there is no need to identify each loop by its nest. The mutual inductances between loops within the same nest are positive because they overlap, while those from different nests do not overlap and are negative: (see (31) and (32)) (see (32) and (33)) (see (33) and (34)) (see (34))

$$\boldsymbol{R_r} = \begin{bmatrix} R_{r_1} + 5R_{\mathrm{e}} & 3R_{\mathrm{e}} & R_{\mathrm{e}} & 0 & 0 & 0 & \cdots & -5R_{\mathrm{e}} \\ 3R_{\mathrm{e}} & R_{r_2} + 3R_{\mathrm{e}} & R_{\mathrm{e}} & 0 & 0 & 0 & \cdots & -3R_{\mathrm{e}} \\ R_{\mathrm{e}} & R_{\mathrm{e}} & R_{r_3} + R_{\mathrm{e}} & 0 & 0 & 0 & \cdots & -R_{\mathrm{e}} \\ 0 & 0 & 0 & R_{r_1} + 5R_{\mathrm{e}} & 3R_{\mathrm{e}} & R_{\mathrm{e}} & \cdots & -5R_{\mathrm{e}} \\ 0 & 0 & 0 & 3R_{\mathrm{e}} & R_{r_2} + 3_e & R_{\mathrm{e}} & \cdots & -3R_{\mathrm{e}} \\ 0 & 0 & 0 & R_{\mathrm{e}} & R_{\mathrm{e}} & R_{r_3} + R_{\mathrm{e}} & \cdots & -R_{\mathrm{e}} \\ \vdots & \vdots & \vdots & \vdots & \vdots & \vdots & \ddots & \vdots \\ -5R_{\mathrm{e}} & -3R_{\mathrm{e}} & -R_{\mathrm{e}} & -5R_{\mathrm{e}} & -3R_{\mathrm{e}} & -R_{\mathrm{e}} & \cdots & n_r R_{\mathrm{e}} \end{bmatrix} \tag{31}$$

$$\boldsymbol{R_r} = \begin{bmatrix} 2R_{\mathrm{b}} + 5R_{\mathrm{e}} + R_{\mathrm{er}} & 3R_{\mathrm{e}} & R_{\mathrm{e}} & -R_{\mathrm{b}} & 0 & 0 & \cdots & -5R_{\mathrm{e}} \\ 3R_{\mathrm{e}} & R_{r_2} + 3R_{\mathrm{e}} & R_{\mathrm{e}} & 0 & 0 & 0 & \cdots & -3R_{\mathrm{e}} \\ R_{\mathrm{e}} & R_{\mathrm{e}} & R_{r_3} + R_{\mathrm{e}} & 0 & 0 & 0 & \cdots & -R_{\mathrm{e}} \\ -R_{\mathrm{b}} & 0 & 0 & 2R_{\mathrm{b}} + 5R_{\mathrm{e}} + R_{\mathrm{er}} & 3R_{\mathrm{e}} & R_{\mathrm{e}} & \cdots & -5R_{\mathrm{e}} \\ 0 & 0 & 0 & 3R_{\mathrm{e}} & R_{r_2} + 3R_{\mathrm{e}} & R_{\mathrm{e}} & \cdots & -3R_{\mathrm{e}} \\ 0 & 0 & 0 & R_{\mathrm{e}} & R_{\mathrm{e}} & R_{r_3} + R_{\mathrm{e}} & \cdots & -R_{\mathrm{e}} \\ . & . & . & -R_{\mathrm{b}} & . & . & \cdots & . \\ \vdots & \vdots & \vdots & \vdots & \vdots & \vdots & \ddots & \vdots \\ -5R_{\mathrm{e}} & -3R_{\mathrm{e}} & -R_{\mathrm{e}} & -5R_{\mathrm{e}} & -3R_{\mathrm{e}} & -R_{\mathrm{e}} & \cdots & n_r R_{\mathrm{e}} \end{bmatrix} \tag{32}$$

$$\boldsymbol{L_r} = \begin{bmatrix} L_{r_{11}} + L_{l_1} + 5L_{\mathrm{e}} & L_{r_{12}} + 3L_{\mathrm{e}} & L_{r_{13}} + L_{\mathrm{e}} & L_{r_{1,1}} & L_{r_{1,2}} & L_{r_{1,3}} & \cdots & -5L_{\mathrm{e}} \\ L_{r_{21}} + 3L_{\mathrm{e}} & L_{r_{22}} + L_{l_2} + 3L_{\mathrm{e}} & L_{r_{23}} + L_{\mathrm{e}} & L_{r_{2,1}} & L_{r_{2,2}} & L_{r_{2,3}} & \cdots & -3L_{\mathrm{e}} \\ L_{r_{31}} + L_{\mathrm{e}} & L_{r_{32}} + L_{\mathrm{e}} & L_{r_{33}} + L_{l_3} + L_{\mathrm{e}} & L_{r_{3,1}} & L_{r_{3,2}} & L_{r_{3,3}} & \cdots & -L_{\mathrm{e}} \\ L_{r_{1,1}} & L_{r_{1,2}} & L_{r_{1,3}} & L_{r_{11}} + L_{l_1} + 5L_{\mathrm{e}} & L_{r_{12}} + 3L_{\mathrm{e}} & L_{r_{13}} + L_{\mathrm{e}} & \cdots & -5L_{\mathrm{e}} \\ L_{r_{2,1}} & L_{r_{2,2}} & L_{r_{2,3}} & L_{r_{21}} + 3L_{\mathrm{e}} & L_{r_{22}} + L_{l_2} + 3L_{\mathrm{e}} & L_{r_{23}} + L_{\mathrm{e}} & \cdots & -3L_{\mathrm{e}} \\ L_{r_{3,1}} & L_{r_{3,2}} & L_{r_{3,3}} & L_{r_{31}} + L_{\mathrm{e}} & L_{r_{32}} + L_{\mathrm{e}} & L_{r_{33}} + L_{l_3} + L_{\mathrm{e}} & \cdots & -L_{\mathrm{e}} \\ \vdots & \vdots & \vdots & \vdots & \vdots & \vdots & \ddots & \vdots \\ -5L_{\mathrm{e}} & -3L_{\mathrm{e}} & -L_{\mathrm{e}} & -5L_{\mathrm{e}} & -3L_{\mathrm{e}} & -L_{\mathrm{e}} & \cdots & n_r L_{\mathrm{e}} \end{bmatrix} \tag{33}$$

$$\boldsymbol{L_r} = \begin{bmatrix} L_{r_{11}} + 2L_{\mathrm{b}} + 5L_{\mathrm{e}} + L_{\mathrm{er}} & L_{r_{12}} + 3L_{\mathrm{e}} & L_{r_{13}} + L_{\mathrm{e}} & L_{r_{1,1}} - L_{\mathrm{b}} & L_{r_{1,2}} & L_{r_{1,3}} & \cdots & -5L_{\mathrm{e}} \\ L_{r_{21}} + 3L_{\mathrm{e}} & L_{r_{22}} + L_{l_2} + 3L_{\mathrm{e}} & L_{r_{23}} + L_{\mathrm{e}} & L_{r_{2,1}} & L_{r_{2,2}} & L_{r_{2,3}} & \cdots & -3L_{\mathrm{e}} \\ L_{r_{31}} + L_{\mathrm{e}} & L_{r_{32}} + L_{\mathrm{e}} & L_{r_{33}} + L_{l_3} + L_{\mathrm{e}} & L_{r_{3,1}} & L_{r_{3,2}} & L_{r_{3,3}} & \cdots & -L_{\mathrm{e}} \\ L_{r_{1,1}} - L_{\mathrm{b}} & L_{r_{1,2}} & L_{r_{1,3}} & L_{r_{11}} + 2L_{\mathrm{b}} + 5L_{\mathrm{e}} + L_{\mathrm{er}} & L_{r_{12}} + 3L_{\mathrm{e}} & L_{r_{13}} + L_{\mathrm{e}} & \cdots & -5L_{\mathrm{e}} \\ L_{r_{2,1}} & L_{r_{2,2}} & L_{r_{2,3}} & L_{r_{21}} + 3L_{\mathrm{e}} & L_{r_{22}} + L_{l_2} + 3L_{\mathrm{e}} & L_{r_{23}} + L_{\mathrm{e}} & \cdots & -3L_{\mathrm{e}} \\ L_{r_{3,1}} & L_{r_{3,2}} & L_{r_{3,3}} & L_{r_{31}} + L_{\mathrm{e}} & L_{r_{32}} + L_{\mathrm{e}} & L_{r_{33}} + L_{l_3} + L_{\mathrm{e}} & \cdots & -L_{\mathrm{e}} \\ . & . & . & L_{r_{1,1}} - L_{\mathrm{b}} & . & . & . & . \\ \vdots & \vdots & \vdots & \vdots & \vdots & \vdots & \ddots & \vdots \\ -5L_{\mathrm{e}} & -3L_{\mathrm{e}} & -L_{\mathrm{e}} & -5L_{\mathrm{e}} & -3L_{\mathrm{e}} & -L_{\mathrm{e}} & \cdots & n_r L_{\mathrm{e}} \end{bmatrix} \tag{34}$$